Molecular Therapy

Original Article



Targeted silencing of Engrailed-1 reprograms profibrotic fibroblast lineage for scarless wound healing

Xuehan Xu,^{1,2} Luyi Wang,^{1,2} Xinyue Bi,² Tingting Cao,^{1,2} Menghua Gao,^{2,4} Buwei Hu,² Jiafeng Zhong,² Chenlin Ji,^{1,2} Rui Sun,^{2,4} Chengjie Sun,^{2,4} Yanjun Zhao,⁵ Qin Zhou,^{2,4} and Jianjun Cheng^{2,3,4}

¹Zhejiang University, Hangzhou, Zhejiang 310027, China; ²Department of Materials Science and Engineering, Westlake University, Hangzhou, Zhejiang 310030, China; ³Research Center for Industries of the Future, Westlake University, Hangzhou, Zhejiang 310030, China; ⁴Institute of Advanced Technology, Westlake Institute for Advanced Study, Hangzhou, Zhejiang 310024, China; ⁵Tianjin Key Laboratory for Modern Drug Delivery & High Efficiency, School of Pharmaceutical Science & Technology, Faculty of Medicine, Tianjin University, Tianjin 300072, China

Skin wounds typically heal with dysfunctional scarring, a fibrotic process largely driven by Engrailed-1 (En1) lineage-positive fibroblasts (EPFs). However, the potential reversibility of EPFs' profibrotic effects and corresponding therapeutic strategies remain elusive. Here, we develop a nanoscale fibroblastmimic carrier (FibroMC) for targeted delivery of En1-specific small interfering RNA (siEn1) to fibroblasts, aiming to inhibit En1 expression and reverse their profibrotic effects. FibroMC was constructed by functionalizing Food and Drug Administration-approved ionizable lipid nanoparticles with fibroblast cell membrane. With incorporated cell membrane proteins (e.g., Integrin β1 and N-cadherin), FibroMC was preferentially taken up by fibroblasts, leading to potent silencing of En1 in all EPF populations both in vitro and in vivo. Consequently, FibroMC treatment significantly inhibited collagen I expression and myofibroblast differentiation. A single dose of topical application of FibroMC to the wound effectively restored collagen architecture, regenerated skin appendages, recovered skin mechanical property, and ultimately prevented scar formation. Our findings demonstrate that FibroMC-mediated En1 silencing can reverse the profibrotic effect of EPFs, offering a promising therapeutic strategy for scarless wound healing.

INTRODUCTION

Skin wounds generally heal with scarring, which differs from normal skin in structure and function. ¹ Unlike healthy skin, scar tissue comprises excessive fibrotic tissue and lacks dermal appendages (e.g., hair follicles and sweat glands), often resulting in disfigurement, impaired mobility, and permanent loss of skin function, significantly impacting the quality of patients' lives. The socioeconomic impact of scar is substantial, with over 100 million new scars forming annually in the United States alone. ² The global economic burden of scarring is estimated to exceed \$64 billion by 2032. ³ However, current clinical practices, such as laser therapy and cryotherapy, among others, primarily address scar appearance with limited efficacy in restoring normal skin function. ⁴ Moreover, ongoing clinical trials for scar

management exhibit limited efficacy and raise concerns of potential adverse effects, including tumorigenesis and immune dysregulation.⁵ Developing effective strategies for scar prevention remains an unmet clinical need.

Fibroblasts are key mediators of scarring, which produce and remodel the extracellular matrix during wound healing.⁶ Based on Engrailed-1 (En1) expression, two distinct fibroblast subtypes with opposing roles in wound repair have been identified in the dermis. En1 lineage-negative fibroblasts (ENFs) are pro-regenerative, depositing a provisional fibronectin-rich matrix and activating Wnt/Trps1 pathways to restore normal skin structure and appendages.^{7,8} Conversely, En1 lineage-positive fibroblasts (EPFs) are profibrotic, mainly by depositing excessive, dense, and parallel collagen I fibers that form scars. EPFs can originate embryonically from ENFs (eEPFs), constituting ca. 75% of dermal fibroblasts in adult skin.⁹ Additionally, En1 can be postnatally activated in ENFs following injury, leading to the conversion into postnatally derived EPFs (pEPFs). 10 This conversion, along with existing eEPFs, results in EPF dominance at the wound site, subsequent excessive collagen I deposition, and scar formation. 11,12 The current work primarily focuses on promoting ENF-mediated scarless wound healing by suppressing postnatal En1 transition through the Yes-associated protein (YAP) inhibitor, verteporfin. 13-15 However, this approach overlooks the significant contribution of eEPFs to the fibrotic process, yielding limited therapeutic effect. 16 Alternatively, complete ablation of the EPF (eEPFs and pEPFs) is not a viable solution either. While this approach prevents scarring, it is accompanied by delayed wound healing and comparable tensile strength to scar tissue, suggesting

Received 15 February 2025; accepted 18 July 2025; https://doi.org/10.1016/j.ymthe.2025.07.031.

Correspondence: Qin Zhou, Department of Materials Science and Engineering, Westlake University, Hangzhou, Zhejiang 310030, China.

E-mail: zhouqin@westlake.edu.cn

Correspondence: Jianjun Cheng, Department of Materials Science and Engineering, Westlake University, Hangzhou, Zhejiang 310030, China.

E-mail: chengjianjun@westlake.edu.cn



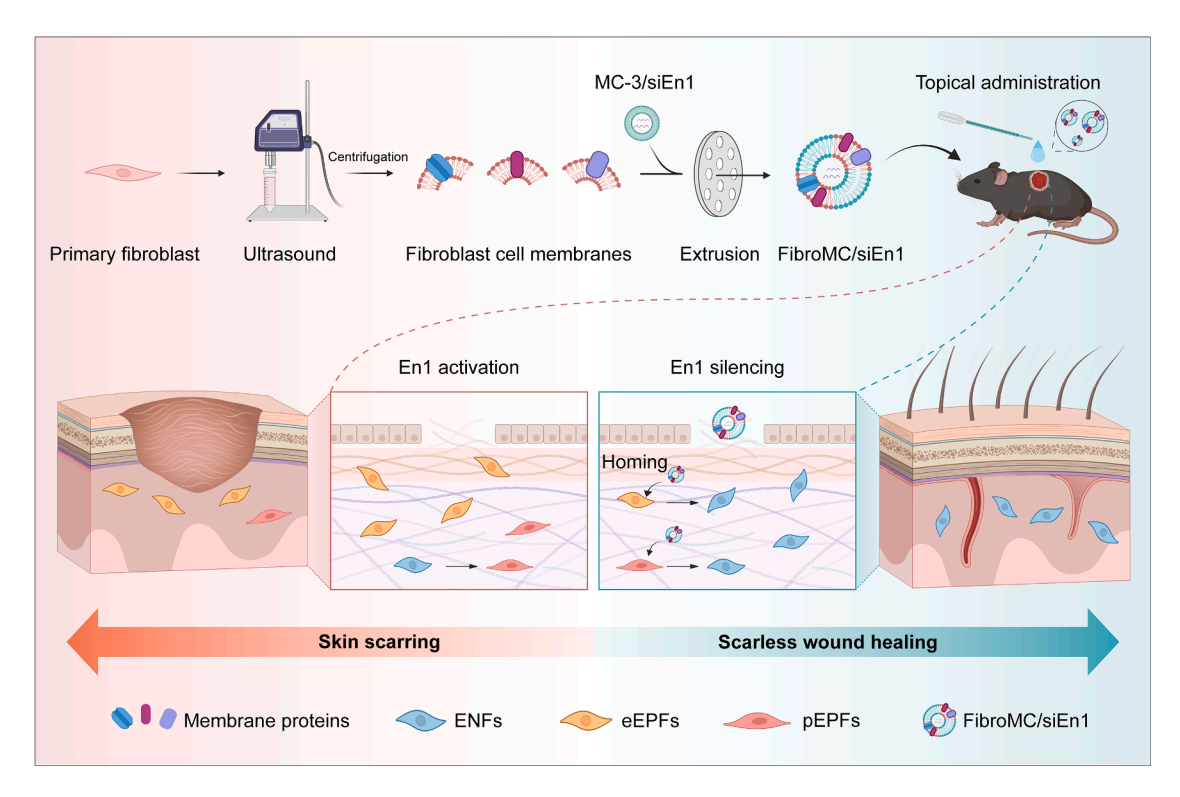


Figure 1. Illustration of scarless wound healing via fibroblast-mimic nanocarriers (FibroMC)-mediated Engrailed-1 silencing and reverse the profibrotic effects of EPFs

En1, Engrailed-1; ENFs, En1 lineage-negative fibroblasts; eEPFs, embryonically En1 lineage-positive fibroblasts; pEPFs, postnatally En1 lineage-positive fibroblasts; siEn1, En1-specific siRNA; MC-3, lipid nanoparticle-containing ionizable DLin-MC3-DMA.

EPFs are profibrotic yet also contribute to wound repair and regeneration. ¹⁰ Reversing the profibrotic effects of EPFs represents an appealing strategy for scarless wound healing.

Small interfering RNA (siRNA) offers a powerful approach to achieve this goal. By specifically silencing the target genes, siRNA has demonstrated the ability to alleviate or reverse pathological processes in various diseases, including transthyretin amyloidosis, and acute hepatic porphyria. The Given the distinct function of ENFs and EPFs, we hypothesized that silencing En1 could reverse the profibrotic effects of EPFs and prevent scar formation. Here, we propose a nanoscale fibroblast-mimic carrier (FibroMC), composed of fibroblast cell membrane-functionalized ionizable lipid nanoparticles, for efficient delivery of En1-specific siRNA (siEn1) to EPFs (Figure 1). FibroMC-mediated siEn1 delivery significantly silences En1 expression in all EPF populations, decreasing collagen I expression and myofibroblast differentiation both *in vitro* and *in vivo*. These findings suggest that FibroMC-mediated En1 silencing can reverse the profibrotic effect of EPFs and prevent scarring.

RESULTS

Engineering FibroMC for efficient siRNA delivery to fibroblasts

Efficient siRNA delivery to fibroblasts is hindered by their inherently low transfection efficiency, diverse fibroblast subtype, and poor cell

uptake. ^{18,19} To address these challenges, we engineered FibroMC, a novel siRNA delivery system inspired by the cell membrane-derived biomimic vesicles. ²⁰ FibroMC is fabricated by incorporating fibroblast cell membranes (FCM) into ionizable lipid nanoparticles (Figure 2A). The fibroblast cell membrane is expected to inherit the homing effect for the enhanced siRNA delivery to fibroblasts. DLin-MC3-DMA-based ionizable lipid nanoparticle (MC-3) was chosen to achieve efficient siRNA encapsulation and lysosomal escape. MC-3 was formulated using the same composition through mimicking the Food and Drug Administration (FDA)-approved siRNA medicine, patisiran (Onpattro).

The Förster resonance energy transfer (FRET) technique was employed to screen the optimal fusion conditions. In detail, DiI-labeled FCM and DiO-labeled MC-3 were fused at different ratios (Figure 2B). The 1:2 (w/w) ratio of fibroblast cell membrane protein to DLin-MC3-DMA ionizable lipid displayed the highest FRET efficiency, indicating the optimal fusion of MC-3 and fibroblast cell membrane. Hence, the ratio of 1:2 was fixed for the subsequent experiments. Super-resolution microscopy was employed to visualize the fusion of FCM and MC-3. The colocalization of the red fluorescence (FCM) and green fluorescence (MC-3) was also observed in FibroMC post extrusion (Figure 2C), illustrating the excellent fusion of lipid films and fibroblast membranes, which is similar to previous

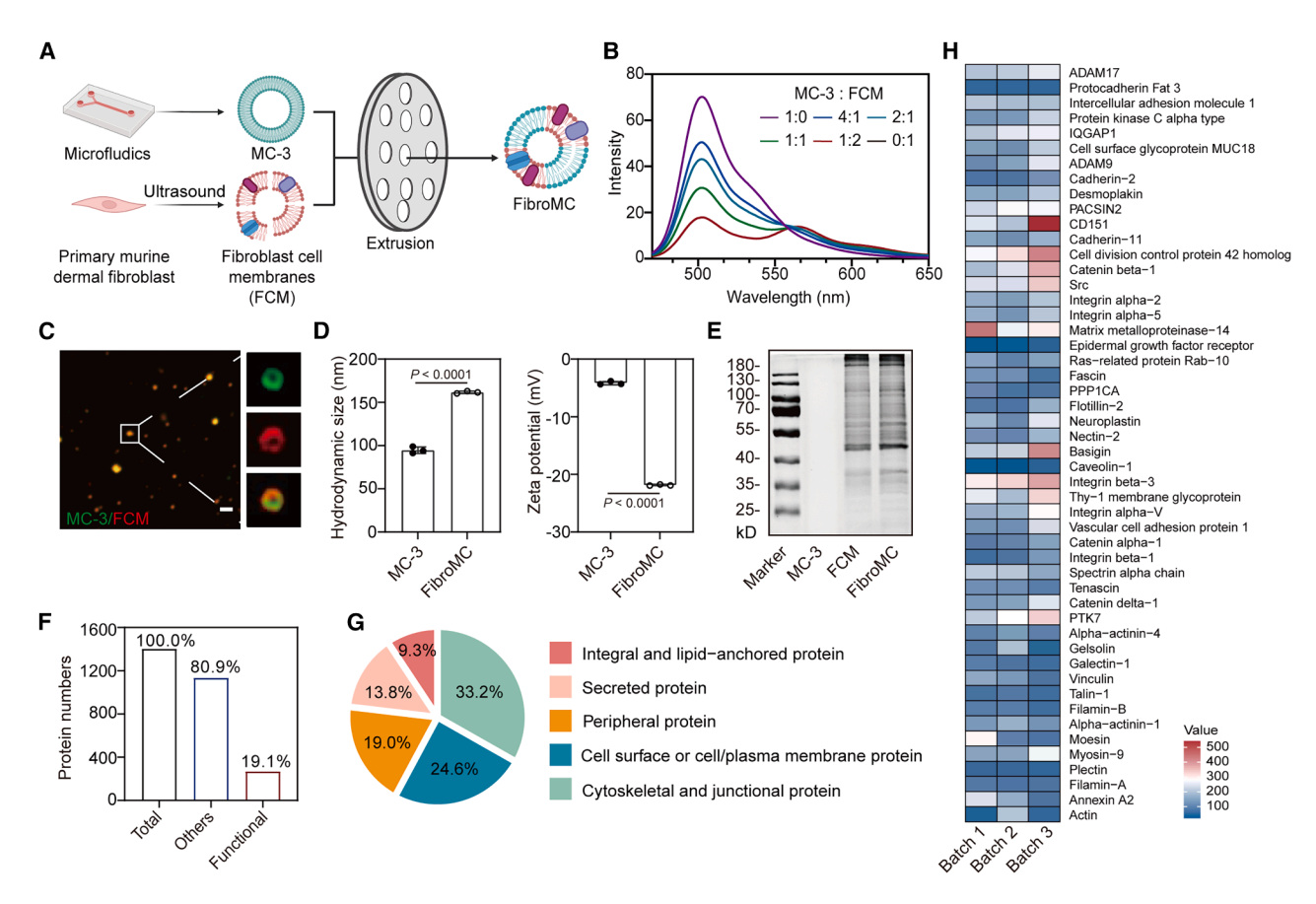


Figure 2. Engineering FibroMC for efficient siRNA delivery to fibroblasts

(A) Schematic illustration describing the design of fibroblast-mimic nanocarrier (FibroMC). (B) The screening of the optimal weight-based fusion ratio between DLin-MC3-DMA-based ionizable lipid nanoparticle (MC-3) and fibroblast cell membrane (FCM) in FibroMC through the Förster resonance energy transfer (FRET) technique. MC-3 and FCM were labeled with DiO and DiI, respectively (Ex = 440 nm). (C) Super-resolution microscopy images of FibroMC fused by FCM (red) and MC-3 (green). Scale bar, 200 nm. (D) Average hydrodynamic size (left) and zeta potential (right) of MC-3, FCM, and FibroMC. (E) SDS-PAGE analysis of MC-3, FCM, and FibroMC to assess membrane protein retention. (F) The proportion of identified 1,402 proteins (total) in FibroMC. Functional proteins referred to those associated with "cell adhesion" or "junction." (G) A pie chart of the functional proteins identified in (F) according to UniProt/GO information. (H) Membrane proteins on FibroMC associated with "cell adhesion" or "cell-cell junction" were detected using tandem mass tag (TMT) based proteomic analysis. Batch1, Batch2, and Batch3 represent three batches of FibroMC samples. Statistical analysis was calculated using the Student's t test (n ≥ 3).

studies.^{21,22} Moreover, the hydrodynamic size of FibroMC was significantly larger than that of MC-3 upon fusion, accompanied by the reversal of the surface charge (Figure 2D).

To verify the retention of membrane proteins during the fusion process, the FibroMC was assessed by sodium dodecyl sulphate-polyacrylamide gel electrophoresis (SDS-PAGE) followed by Coomassie brilliant blue staining (Figure 2E). The protein profile of FibroMC closely resembled that of the FCM, indicating the successful incorporation of fibroblast membrane proteins. Additionally, three independent batches of FibroMC were examined by proteomic profiling using the tandem mass tag (TMT) strategy. Only minor batch-to-batch variations were observed (Figure S1A). Across all these batches, 1,402 proteins were identified with varying molecular weights (Figures 2F and S1B). Gene ontology (GO) enrichment analysis suggested that 268 of these proteins (19.1% of the 1,402 proteins, marked

as functional proteins, Figure 2F) are associated with cell adhesion or junction (Figure S1C). These proteins include integral and lipid-anchored (9.3%), secreted (13.8%), peripheral (19.0%), cell surface or cell/plasma membrane (24.6%), and cytoskeletal or junctional proteins (33.2%), which is similar to what was reported for other types of cells^{23,24} (Figure 2G). The top 50 relative proteins are visualized in the heatmap (Figure 2H). Several proteins involved in cell-cell interaction, such as Integrin α 2, β 1, β 3, N-cadherin, and OB-cadherin, were detected in FibroMC, which may contribute to efficient siRNA delivery to fibroblasts.

Moreover, the components of clinically approved lipid nanoparticles were used to load siRNA and fuse with cell membranes for active targeting. We found that different N/P ratios (3–9) do not affect siRNA encapsulation (Figure S2A). Therefore, we adopted the FDA-approved formulation ratio for subsequent studies. The obtained FibroMC

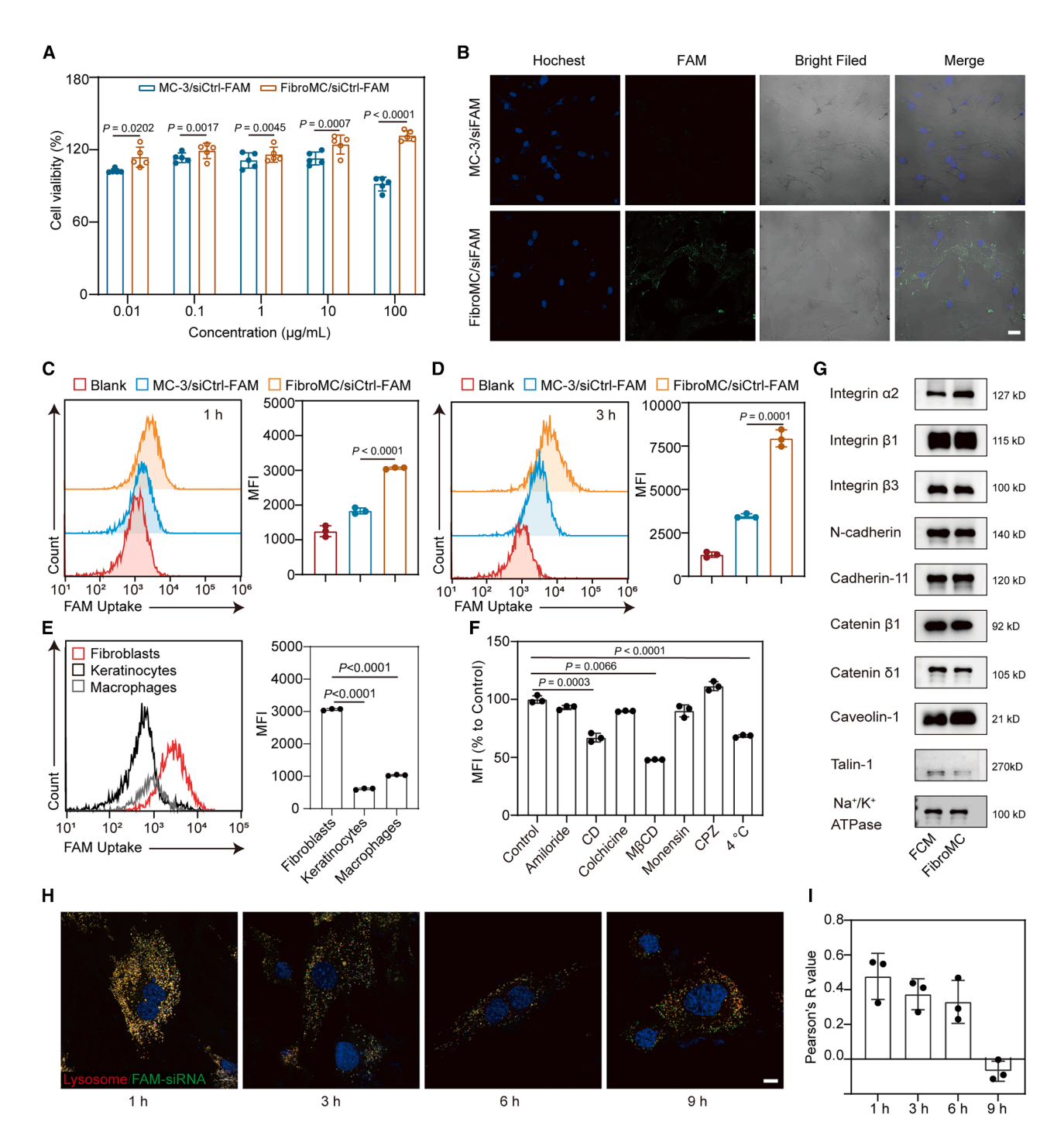


Figure 3. Cell membrane proteins enhanced the affinity between FibroMC and fibroblasts

(A) Viability of fibroblasts upon incubation with siCtrl-FAM-loaded MC-3 (MC-3/siCtrl-FAM) and siCtrl-FAM-loaded FibroMC (FibroMC/siCtrl-FAM) for 48 h. (B) Representative confocal microscopy images of fibroblasts after 1-h incubation with MC-3/siCtrl-FAM and FibroMC/siCtrl-FAM. Scale bar, 40 μm. (C and D) Flow cytometry analysis of indicated siCtrl-FAM-loaded nanocarriers in fibroblasts after incubation for 1 h or 3 h, and the corresponding quantification of the mean fluorescence intensity. (E) Flow cytometry comparison and statistical comparison of indicated siCtl-FAM-loaded nanocarriers on keratinocytes, RAW264.7 cells, and fibroblasts after incubation for 1 h. (F) The influence of endocytosis inhibitors on FibroMC/siCtrl-FAM nanocarrier uptake by fibroblasts. The relative fluorescence intensity of FAM was quantified by flow cytometry and normalized to FibroMC/siCtrl-FAM without treatment after treatment with the following conditions or inhibitors: 4°C (energy-dependent endocytosis), amiloride (macropinocytosis), cytochalasin D (phagocytosis), colchicine (microtubules depolymerization), MβCD (caveolae-mediated endocytosis), and chlorpromazine/CPZ

nanocarrier exhibited a spherical morphology (Figure S2B) with a high encapsulation efficiency of 99.3% (Figure S2C), robust protection of the encapsulated siRNA from degradation (Figure S2D), and good stability (Figure S2E), which is comparable to siRNA-loaded MC-3 lipid nanoparticles. Collectively, these results suggested that FibroMCs were successfully constructed with the surface deposition of functional fibroblast cell membrane proteins, and the siRNA encapsulation through MC-3. This suggests the potential of FibroMCs for highly efficient siRNA delivery to fibroblasts.

Cell membrane proteins enhanced the affinity between FibroMC and fibroblasts

The potency of FibroMC depends on its affinity with fibroblasts. To assess the interaction between FibroMC and fibroblasts, fluorescent probe (FAM)-labeled control siRNA was loaded into MC-3 (MC-3/ siCtrl-FAM) and FibroMC (FibroMC/siCtrl-FAM) nanocarriers. FibroMC/siCtrl-FAM displayed no cytotoxicity in primary mouse dermal fibroblasts at concentrations up to 100 µg/µL, whereas MC-3/siCtrl-FAM significantly reduced the cell viability under the same conditions (Figure 3A). This can be explained by the presence of ionizable lipids (DLin-MC3-DMA). Next, the cellular uptake of FibroMC/siCtrl-FAM by fibroblasts was analyzed by flow cytometry (FACS). FibroMC/siCtrl-FAM displayed enhanced fluorescence intensity (1.7-fold) compared with MC-3/siCtrl-FAM at 1 h post incubation with fibroblasts (Figures 3B and 3C). Quantitative FACS results were consistent with the above conclusion; the extent of uptake was 35.6% \pm 1.3% (FibroMC/siCtrl-FAM) and 5.9% \pm 1.6% (MC-3/siCtrl-FAM), respectively (Figure S3A). Meanwhile, the internalization of FibroMC/siCtrl-FAM in fibroblasts was time-dependent; at 3 h post incubation, the intracellular fluorescence intensity of FibroMC/siCtrl-FAM in reference to MC-3/siCtrl-FAM increased to 2.2 (Figure 3D). Furthermore, we investigated the influence of fibroblast membrane composition on the uptake of FibroMC by keratinocytes and macrophages in the skin. In contrast to fibroblasts, these cells exhibited minimal uptake of FibroMC/siCtl-FAM, as evidenced by the low fluorescence intensity determined by FACS (Figures 3E and S3B), demonstrating the preferential uptake of FibroMC by fibroblasts.

Co-treatment with cytochalasin D (a phagocytosis inhibitor) or M β CD (caveolae-mediated endocytosis inhibitor) significantly decreased the mean fluorescence intensity (MFI); likewise, reducing the culturing temperature to 4°C showed the same phenomena (Figure 3F). These data indicate that caveolae/raft-mediated energy-dependent endocytosis and phagocytosis are the primary mechanisms contributing to the cellular uptake of FibroMC in fibroblasts. Subsequently, we investigated the role of membrane proteins in FibroMC internalization through the approach of antibody-targeted protein blocking. We selected Integrin α 2, β 1, β 3, N-cadherin,

Cadherin-11, Catenin β1, delta1, Caveolin-1, and Talin-1, all of which are typical proteins involved in cell-cell interaction (Figure 3G). Trypsin treatment served as a positive control to extensively digest the membrane proteins. Among these selected proteins, blocking Integrin \(\beta 1, \text{ } \beta 3, \text{ N-cadherin, and Talin-1 significantly } \) reduced the fluorescence intensity of fibroblasts, suggesting the collective contribution of multiple proteins to the affinity between FibroMC and fibroblasts (Figure S3C). Beyond the high affinity between FibroMC and fibroblasts, potent gene silencing also requires efficient siRNA escape from lysosomes.²⁶ Both MC-3 and FibroMC nanocarriers exhibited time-dependent lysosomal escape, evidenced by the reduced Pearson's correlation coefficient (R) (Figures 3H, 3I, and S4). After a 9-h incubation, the negative R value regarding FibroMC suggested that siCtrl-FAM almost wholly escaped from the lysosome, indicating their promising capability for effective gene silencing.

FibroMC-mediated En1 silencing reverses the profibrotic effect of EPFs in vitro

Efficient EPF sorting is essential to assess the in vitro efficacy of En1 silencing. Previous studies identified CD26 as a surface marker for EPFs, based on which we specifically sorted eEPFs and ENFs according to the level of CD26 expression (Figures 4A, S5A, and S5B). pEPFs were generated via activating ENFs with a YAP activator, PY-60.²⁷ Verteporfin, a YAP inhibitor, was used as the positive control. siEn1 was loaded in MC-3 (MC-3/siEn1) and FibroMC (FibroMC/siEn1) nanocarriers, respectively. Next, EPFs were incubated with either FibroMC/siEn1 or MC-3/siEn1. Quantitative reverse transcription polymerase chain reaction (RT-qPCR) and western blotting were employed to quantify En1 mRNA and protein expression. At 12 h post treatment, FibroMC/siEn1 significantly downregulated En1 mRNA level in all EPF populations (eEPFs and pEPFs) compared with MC-3/siEn1 (Figures 4B and 4D), confirming its superior uptake efficiency by fibroblasts. At 48 h, although mRNA levels were similar between the two groups (Figure S6), western blotting revealed that FibroMC/siEn1 induced a marked reduction in En1 protein levels in all EPFs (Figures 4F and 4G), indicating its sustained silencing efficacy.

We next examined whether siRNA-mediated En1 silencing could attenuate the profibrotic effects of EPFs. The fibrotic response was evaluated using collagen I and α -smooth muscle actin (α -SMA), a marker of myofibroblasts. Both markers are critical indices of fibrosis. Collagen I represents the main component of scar tissue, and α -SMA is associated with myofibroblast activation, which is a vital mediator of excessive tissue contraction and extracellular matrix deposition during scarring. SiRNA-mediated En1 silencing significantly decreased collagen I expression in EPFs, as indicated by lower levels of *Col1a1* and *Col1a2* mRNA, and decreased collagen I protein

(clathrin-mediated inhibitor). (G) Representative western blots of membrane proteins in the fibroblast cell membrane and FibroMC nanocarrier. (H) Intracellular distribution of FibroMC/siCtrl-FAM nanocarrier (green) in fibroblasts. Nuclei were stained with DAPI (blue), and lysosomes were labeled with LysoTracker Red DND-99 (red), respectively. Scale bar, 10 μ m. (I) Pearson's correlation coefficient of the fluorescence colocalization between FAM and LysoTracker Red DND-99 in fibroblasts, as calculated using ImageJ software. Data are presented as the mean \pm standard deviation (SD). Statistical analysis was calculated using the Student's t test ($n \ge 3$).

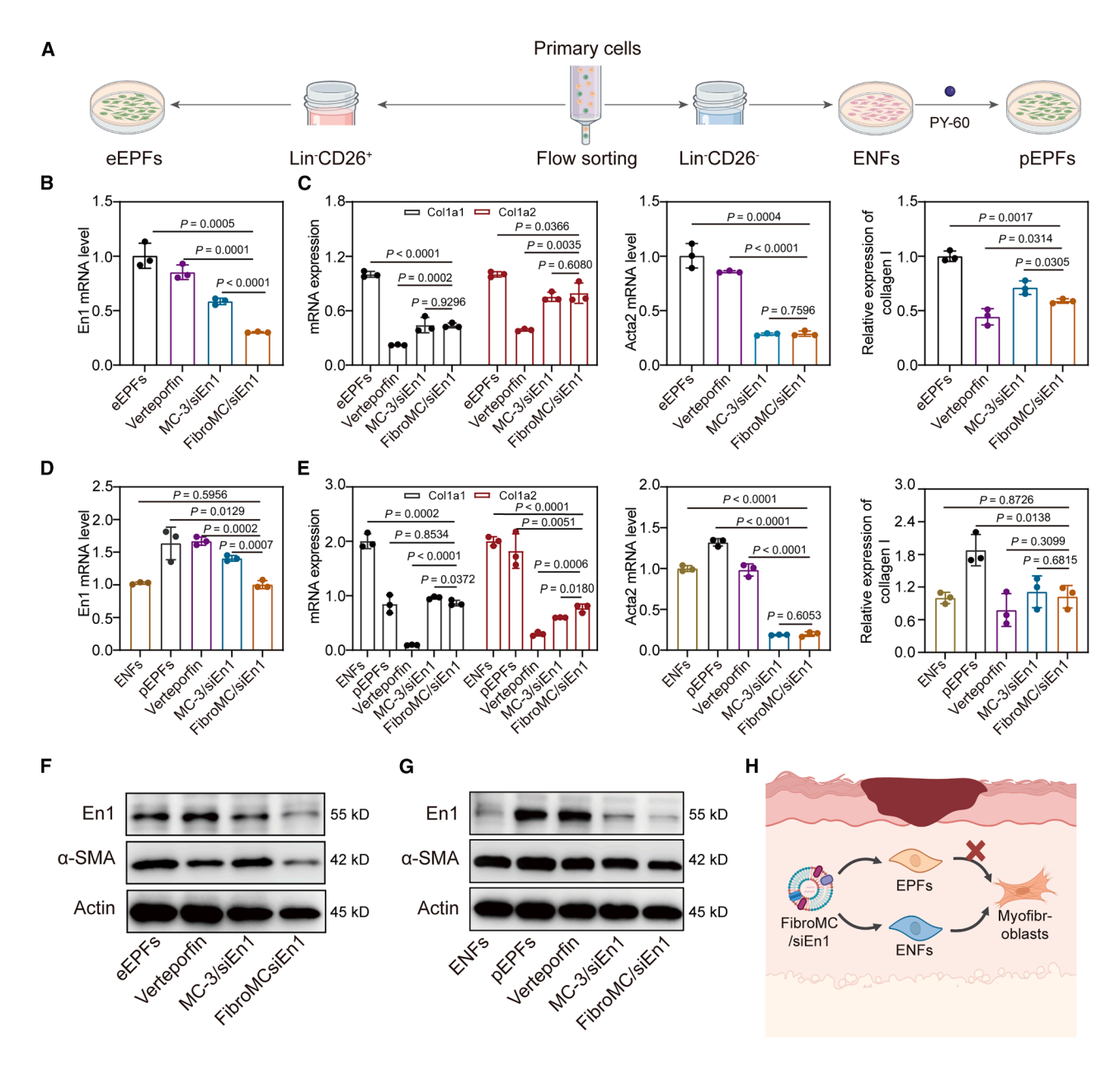


Figure 4. FibroMC-mediated En1 silencing reverses the profibrotic effect of EPFs in vitro

(A) Schematic of embryonic EPF (eEPF) isolation and postnatal EPF (pEPF) induction. Lineage-negative cells (Lin⁻: CD31⁻, CD45⁻, Ter119⁻, Tie2⁻ EpCam⁻). (B) Relative *En1* mRNA expression levels in eEPFs following a 12-h treatment with three formulations (verteporfin, MC-3/siEn1, and FibroMC/siEn1). (C) Relative *Col1a1*, *Col1a2*, and *Acta2* mRNA and collagen I protein levels in eEPFs post treatment with three formulations. (D) Relative *En1* mRNA levels in pEPFs following a 12-h treatment with three formulations. (E) Relative *Col1a1*, *Col1a2*, and *Acta2* mRNA and collagen I protein levels in pEPFs post treatment with three formulations. (F) Representative western blots of En1 and α -SMA in eEPFs after treatment with different formulations for 48 h. (H) Schematic illustration showing that En1 knockdown promotes ENF-mediated myofibroblast differentiation. Statistical analysis was calculated using the Student's t test ($n \ge 3$).

following treatment with FibroMC/siEn1. Moreover, En1 silencing prevented the fibroblast-to-myofibroblast transition in EPFs, as evidenced by the reduced levels of Acta2 mRNA and α -SMA protein (Figures 4C and 4E–4G). However, En1 silencing exerted negligible effects on ENFs, as evidenced by their unaltered viability, migration

capacity, and fibronectin expression (Figure S7). Furthermore, FibroMC/siEn1 treatment did not affect the differentiation of fibroblasts into myofibroblasts (Figure S8). This suggests the potential of ENFs-mediated myofibroblast differentiation upon En1 silencing (Figure 4H). Additionally, verteporfin exhibited an unexpected

impact on EPFs. It did not affect En1 expression and myofibroblast activation in eEPFs and pEPFs, while showing a more potent inhibitory effect in collagen I expression compared with siRNA treatment. Regarding eEPFs, we presumed that YAP-dependent activation of En1 had already occurred during the embryonic stage of these cells. As for pEPFs, this might be due to verteporfin's pleiotropic action beyond En1.²⁹ These findings demonstrated that FibroMC/siEn1 could efficiently knockdown En1 and reverse the profibrotic effects of EPFs, as evidenced by the diminishment of collagen I expression and myofibroblast differentiation. These *in vitro* data suggested a promising therapeutic effect of FibroMC/siEn1 in skin scarring prevention *in vivo*.

FibroMC-mediated En1 silencing reverses the profibrotic effect of EPFs in vivo

Encouraged by the promising in vitro therapeutic effects of En1 silencing, we further investigated the in vivo performance of FibroMC nanocarrier. Full-thickness skin wounds were established on the back of C57BL/6 mice and the skin was splinted with silicone rings to prevent contraction.³⁰ Subsequently, the wounds were treated with a single dose of phosphate-buffered saline (PBS; Blank), verteporfin, MC-3/siEn1, or FibroMC/siEn1 on day 0, followed by the efficacy assessment for a time course of 2 weeks (Figure 5A). On day 14, immunofluorescence staining was performed to evaluate En1 silencing in the wound area. FibroMC/ siEn1 remarkably knocked down En1, as proved by the significant reduction of En1-positive fluorescence signals (Figures 5B and 5E). Although MC-3/siEn1 and FibroMC/siEn1 exhibited similar potency in silencing En1 in vitro, the latter was significantly more potent in vivo than the counterpart. Such discrepancy can be explained by the FibroMC-mediated efficient delivery of siEn1 to the fibroblasts.

Consequently, FibroMC/siEn1 significantly decreased collagen I expression and myofibroblast differentiation in vivo. The presence and concentration of type I (yellow) and type III (green) collagen were determined by the Sirius red staining. The ratio of type I/III collagen significantly decreased from 9.5 (Control) to 2.2 (FibroMC/siEn1) upon En1 silencing (Figures 5C and 5F). Moreover, treatment by FibroMC/siEn1 exhibited a randomly aligned collagen structure akin to the typical basket weave-like collagen fiber network in normal skin (Figure 5G). Double immunofluorescence staining of α-SMA (myofibroblasts) and vimentin (fibroblasts) was further performed to assess the influence of En1 knockdown in myofibroblasts.³¹ Analysis of the colocalized areas revealed that fewer myofibroblasts were present in the skin tissue treated by FibroMC/ siEn1 (Figures 5D and 5H). Collectively, these results demonstrated that FibroMC-mediated En1 silencing can reverse the profibrotic effect of EPFs and decrease collagen I expression and myofibroblast differentiation in vivo.

FibroMC/siEn1 promotes scarless wound healing in vivo

Given the potency of FibroMC/siEn1 in mitigating fibrosis, its therapeutic efficacy on wound healing was investigated. The gloss

appearance of wound sites across various groups on days 0, 3, 7, and 14 all exhibited gradual healing over the experimental period (Figure S9A). The relative wound area analysis revealed no significant difference among all groups, indicating that FibroMC/siEn1 did not impede wound healing (Figure 6A). FibroMC/siEn1 treatment significantly reduced the scar area on day 14 compared with other formulations (Figures 6B and S9B).

Hematoxylin and eosin (H&E) and Masson's trichrome staining were used to analyze the thickness of the dermis and epidermis, the amount of collagen, and the number of hair follicles and glands. FibroMC/siEn1 treatment increased the thickness of the dermis layer and decreased the epidermal thickness, indicative of effective tissue repair (Figures 6C–6E). This balanced healing response is crucial for preventing the development of functionally and aesthetically problematic keloid scars.³² Quantitative evaluation of collagen volume fraction corroborated the observed dermal thickness, confirming the enhanced capability of FibroMC/siEn1 to deposit collagen (Figure 6F). Moreover, PBS and verteporfin treatment resulted in thick and densely packed collagen bundles. In contrast, upon FibroMC/siEn1 treatment, we observed thinner and randomly aligned collagen fibers that closely resemble the standard skin architecture (Figures 5G and 6G).

An effective scarless therapy should not only restore normal matrix structure, but also promote the regeneration of skin appendages and skin mechanical property recovery, which is hardly achieved by the current therapies.33 The increased number of newly formed hair follicles (Figures 6B, 6D, and 6H) and glands (Figures 6D and 6I) underscores the improved regenerative healing facilitated by FibroMC/siEn1. Post FibroMC/siEn1 treatment, an increased blood vessel regeneration was observed compared with the control, as evidenced by the CD31 staining images (Figures 6J and 6K). Additionally, immunohistochemistry staining of vascular endothelial growth factor (VEGF) was carried out to assess the mechanism of blood vessel regeneration.³⁴ VEGF expression was significantly higher in the FibroMC/siEn1-treated skin compared with other groups (Figures 6J and 6L). This finding concurred well with the in vitro data that En1-silenced eEPFs secreted more VEGF protein than eEPFs (Figure \$10). Collectively, En1 silencing promotes blood vessel regeneration via enhanced VEGF secretion. The enhanced neovascularization may enable a sufficient supply of nutrients and oxygen, promoting hair follicle and sweat gland regeneration.³⁵ FibroMC/siEn1 also promotes the recovery of skin mechanical property. The tensile strength of healed skin treated with FibroMC/siEn1 recovers to 53.5% of unwounded skin by day 14 and substantially recovers to 73.8% by day 28 (Figure S11). Meanwhile, all the tested mice's body weights increased throughout the experimental period (Figure S12A). There was no pathological change in the major organs of the tested mice based on the H&E staining images (Figure S12B). At the local wound site, key inflammatory cytokines in skin tissues were quantified. The levels of interleukin (IL)-4 and IL-6 remained unchanged in the FibroMC/siEn1-treated group compared with controls. Importantly, the level of the pro-inflammatory cytokine

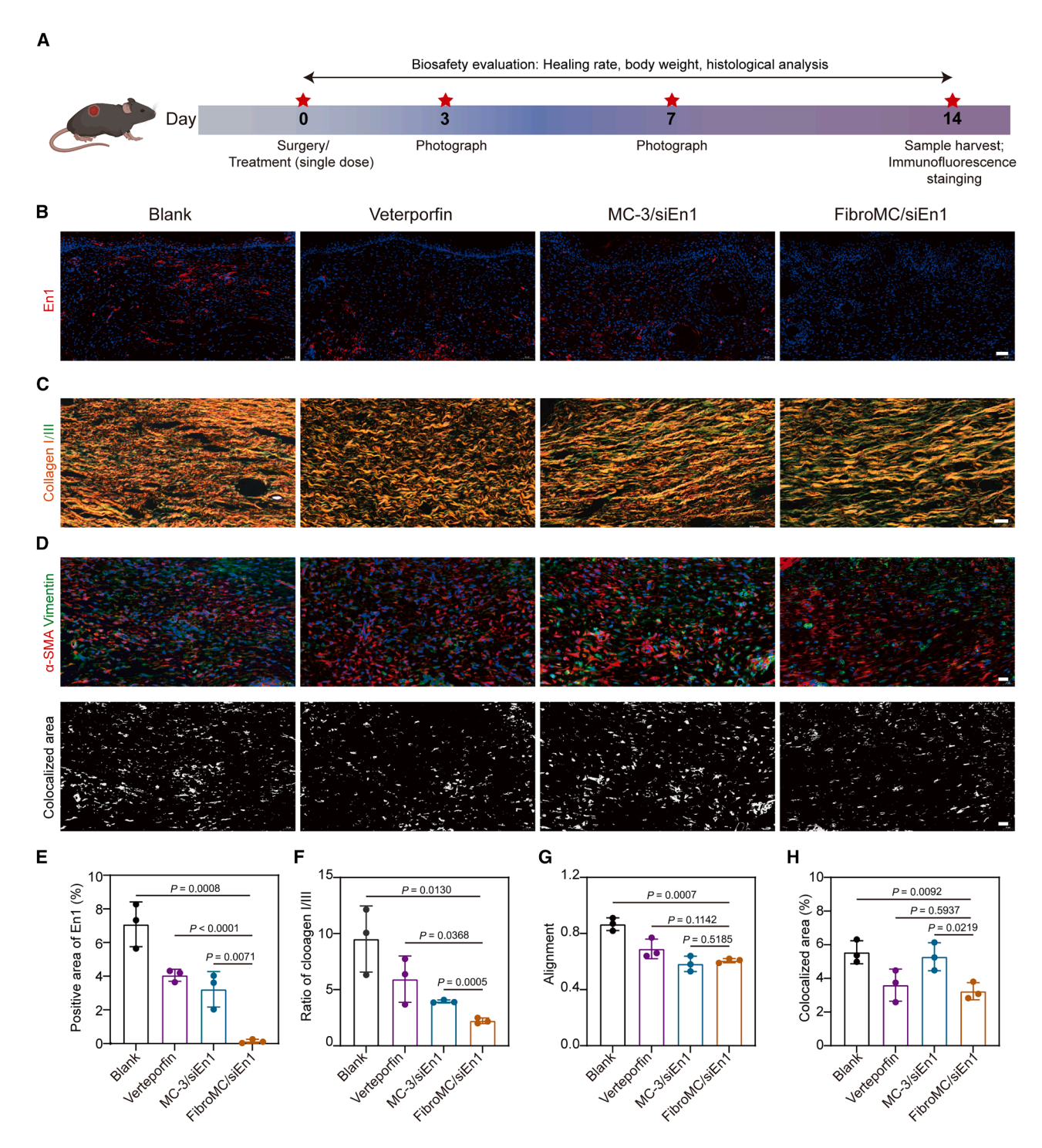


Figure 5. FibroMC-mediated En1 silencing reverses the profibrotic effect of EPFs in vivo

(A) Schematic of the *in vivo* experimental process. (B) Immunofluorescence staining of En1 of wound skin on day 14. Scale bar, 50 μ m. (C) Sirius red staining of wounds on day 14. Yellow indicates collagen I and green indicates collagen III. Scale bar, 25 μ m. (D) Double immunofluorescence staining (up) and colocalized area (bottom) of α -SMA and vimentin of wound skin on day 14. Scale bar, 20 μ m. (E–H) Statistical analysis of the positive area of En1 (E); type I/III collagen ratio (F); collagen alignment (G); and colocalized area indicates the myofibroblast-positive area of CD31 (H). Statistical analysis was calculated using the Student's t test ($n \ge 3$).

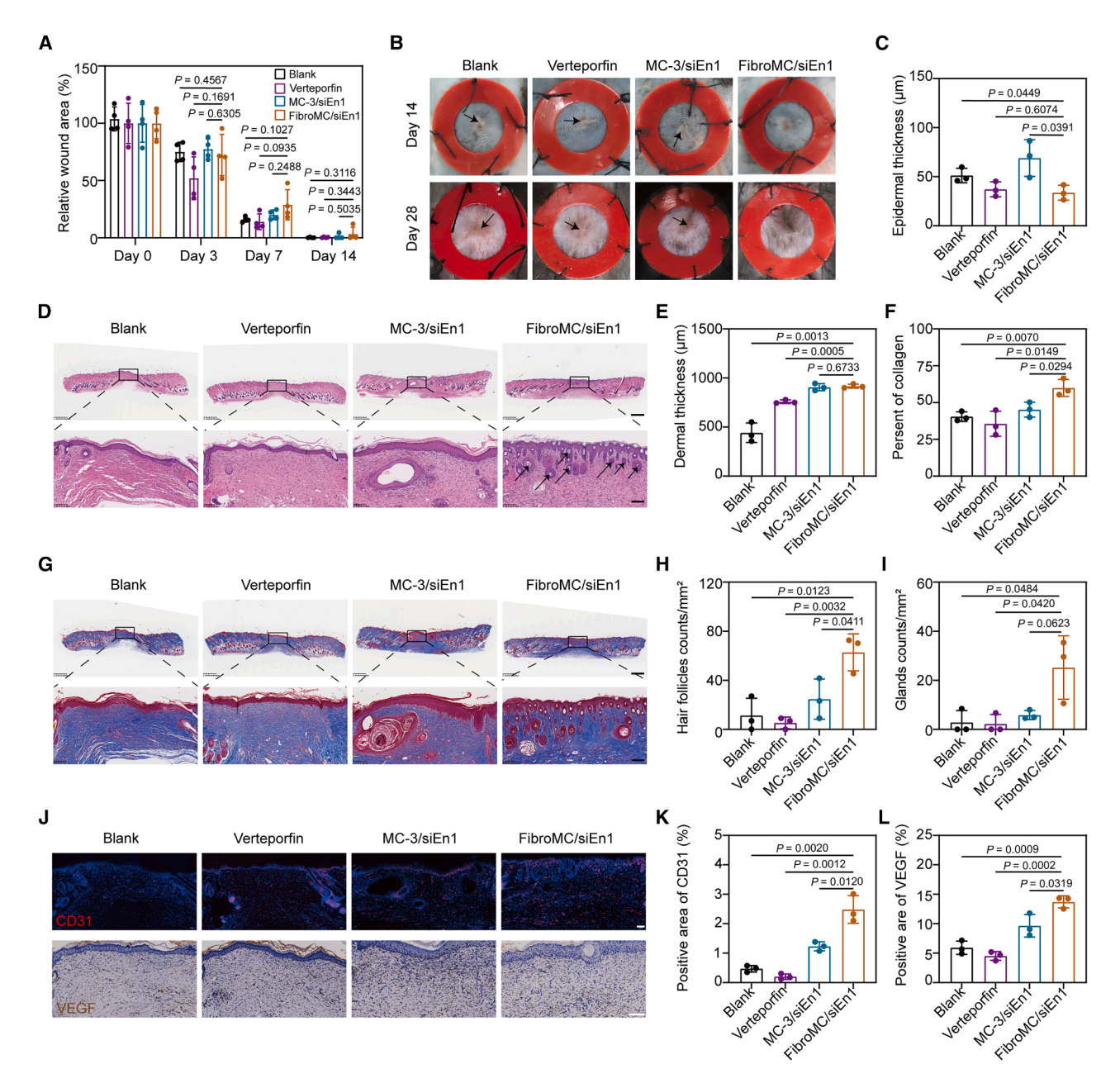


Figure 6. FibroMC/siEn1 promotes scarless wound healing in vivo

(A) Quantitative evaluation and statistical analysis of relative wound size in Blank, Verteporfin, MC-3/siEn1, and FibroMC/siEN1 from day 0 to day 14. (B) Gloss appearance images of the wound sites on days 14 and 28. Black arrow indicates scar area. (C) Statistical analysis of epidermal thickness. (D) Representative H&E staining of wounds on day 14. Scale bar, 625 μ m (top), 100 μ m (enlarged). Black arrow indicates hair follicles. (E) Statistical analysis of dermal thickness. (F) Statistical analysis of the collagen level. (G) Representative Masson trichrome staining of wounds on day 14. Scale bar, 625 μ m (top), 100 μ m (enlarged). Statistical analysis of (H) hair follicles and (I) glands. (J) Immunofluorescence staining of CD31 (top) and immunohistochemical staining of VEGF (bottom) of wound skin on day 14. Scale bar, 100 μ m. Comparison of (K) CD31 and (L) VEGF-positive area. Statistical analysis was performed using the Student's t test ($n \ge 3$).

TNF- α was found to be significantly decreased in skin tissues following FibroMC/siEn1 treatment, indicating a potential anti-inflammatory effect (Figure S13). Collectively, these results demonstrated the biocompatibility of FibroMC/siEn1 for the *in vivo* management of skin disorders.

DISCUSSION

Skin scarring remains a significant clinical challenge. EPFs play a crucial role in the scarring process, and reversing the profibrotic effects of EPFs represents an appealing strategy for scarless wound healing. Current research primarily focuses on promoting

ENF-mediated wound healing for scarless regeneration. Verteporfin has been formulated into nanogels, nanoparticles, and liposomes to prevent scar formation by blocking the conversion from ENF to pEPF. ^{13,15,36,37} However, the therapeutic efficacy of verteporfin is limited as it only partially inhibits pEPF formation (by 40%–50%) and largely neglects the role of eEPFs. ¹⁶ Moreover, verteporfin treatment improves skin structure within 14 days, whereas it exhibits a limited effect on skin appendage regeneration that usually takes months or longer.

In this study, we demonstrate that the profibrotic effect of EPFs can be attenuated via RNA interference, thereby facilitating scarless wound healing. We developed FibroMC, a novel siRNA delivery system for efficient En1 silencing in fibroblasts. By functionalizing FDA-approved ionizable lipid nanoparticles with fibroblast cell membrane, the enhanced siRNA delivery to fibroblasts and lysosomal escape were realized. Mechanistic analysis revealed that enhanced siRNA delivery was attributed to the presence of various cell adhesion proteins in the FibroMC, including, but not limited to, Integrins $\alpha 2$, $\beta 1$, and $\beta 3$, as well as N-cadherin. En1 expression was significantly knocked down in all EPF populations by FibroMC/siEn1, resulting in decreased collagen I expression and myofibroblast differentiation in vitro and in vivo.

Remarkably, topical application of a single dose of FibroMC/siEn1 to the skin wound potently silenced En1, restored the collagen architecture of newly formed skin, and promoted skin appendage regeneration within 14 days. In contrast, it takes up to 90 days to attenuate the scarring during the process of wound healing by using verteporfin therapies combined with microneedles and photothermal approaches. 14 Previous research has also combined verteporfin with macrophage regulation and bacterial inhibition, which increased the therapeutic effect to a certain extent compared with the monotherapy of verteporfin.³⁸ However, the clinical translation of combinational therapies is very challenging due to the increased complexity and associated difficulty in quality control. FibroMC/ siEn1 also promoted the recovery of skin mechanical property, with tensile strength restored to ~73.8% of normal levels. While reduced collagen content may limit full recovery, the improved collagen architecture (Figure 5G) likely contributes to the mechanical improvement. 39,40 Optimizing dosage and frequency may further enhance outcomes by restoring collagen balance.

Besides, our work indicates that verteporfin may inhibit collagen I and α -SMA through the mechanism(s) beyond En1 regulation. In vitro, verteporfin did not affect En1 expression and myofibroblast activation in either eEPFs or pEPFs, but potently inhibited collagen I expression more effectively than siEn1 treatment. However, in vivo, verteporfin reduced En1 expression, decreased myofibroblast activation, and inhibited collagen I expression. Similar results of verteporfin-induced myofibroblast differentiation inhibition have been reported previously. ^{15,36} These discrepant results between in vitro and in vivo data might be due to the pleiotropic effect of verteporfin in vivo; verteporfin may act on YAP and hence stimulate multiple

signaling pathways, e.g., transforming growth factor (TGF)- β and connective tissue growth factor (CTGF), which are crucial for wound healing. The similar phenomenon was also observed in Figure 6C. These results suggest that verteporfin promotes scarless wound healing through a more complex mechanism other than solely preventing En1 activation.

Moreover, verteporfin has been demonstrated to inhibit angiogenesis through the suppression of the YAP/TEAD complex. ⁴⁴ Consistent with this, we confirmed the anti-angiogenic effect of verteporfin, as indicated by the reduction of CD31 fluorescence upon verteporfin treatment. Conversely, FibroMC/siEn1 treatment enhanced blood vessel regeneration, accompanied with elevated VEGF secretion *in vitro* and *in vivo* (Figures 6J, 6L, and S10). Previous studies showed that ENF transplantation could enhance neovascularization⁷; likewise, the data in the current work corroborated that ENF transplantation promoted neovascularization, suggesting that En1-silenced EPFs might adopt ENF-like pro-angiogenic properties. The enhanced neovascularization further provides a more abundant supply of nutrients and oxygen, which would be beneficial for hair follicle⁴⁵ and sweat gland regeneration. ⁴⁶

Our study has some limitations. Identifying the proteins that exhibit the highest affinity for fibroblasts could optimize the FibroMC formulation and enhance targeting efficiency. Nevertheless, it is highly challenging because of the potential synergistic effects between multiple cell membrane-derived proteins. Furthermore, our study demonstrated that the profibrotic effect of EPFs could be modulated, but the mechanism of skin appendage regeneration still requires further investigation. In conclusion, our results demonstrate that FibroMC-mediated En1 silencing can reverse the profibrotic effects of EPFs and promote scarless wound healing. These findings offer a novel approach to scar prevention with potential clinical translation. Given that fibroblast heterogeneity has also been identified in other organs, 47 this strategy may also apply to other fibrotic diseases.

MATERIALS AND METHODS

Isolation of primary murine dermal fibroblasts and keratinocytes

The dorsal skin of C57BL6/J neonates was harvested and washed with Hank's balanced salt solution (HBSS, Solarbio). The skin was minced into small pieces with surgical scissors and washed again with HBSS. After digesting it with Dispase II solution (0.5% in PBS, Yeasen) overnight at 4°C, two curved forceps were used to separate the dermis and epidermis carefully. The murine dermal fibroblasts were generated as follows. The dermis was incubated with Trypsin-EDTA solution for 30 min at 37°C, 5% CO₂ followed by regular shaking. The digested sample was filtered using a 100- μ m nylon filter and centrifuged at 300 × g for 5 min. The pellet was resuspended in Dulbecco's modified Eagle's medium (DMEM) containing 10% fetal bovine serum (FBS) and 1% penicillin/streptomycin and put in culture flasks. The keratinocytes were obtained by incubating the epidermis on a Petri dish in Trypsin-EDTA solution at ambient temperature on a horizontal shaker with gentle agitation for 20 min.

Then, the epidermis was collected using forceps, followed by vigorous rubbing back and forth to release cells from the epidermal sheet. Then the cell suspension was filtered through a 100- μ m filter and centrifuged at 300 × g for 5 min. The pellet was resuspended in EpiLife medium (Gibco) with supplement of EpiLife Defined Growth Supplement (EDGS, Gibco) in culture dishes (NEST Biotechnology) that were pre-coated with attachment factor (Thermo Fisher) to promote cell attachment.

Isolation of eEPFs and ENFs

The isolation of eEPFs and ENFs was carried out based on the published protocols.^{7,9} Briefly, the dorsal skin of C57BL6/J neonates was harvested and washed with HBSS. The skin was minced into small pieces with surgical scissors and washed again with HBSS. Samples were resuspended in 2 mL of digestion solution containing 1 mg mL⁻¹ of collagenase I (Solarbio), 0.5 mg mL⁻¹ of hyaluronidase (Absin), and 25 U mL⁻¹ of DNase I (Thermo Fisher), followed by incubation at 37°C for 30 min with agitation. DMEM (10 mL) containing 10% FBS was added to stop the enzymatic reaction, and the suspension was sequentially filtered through a 100-µm and then 40- μ m cell strainer. After centrifugation at 300 \times g for 5 min, the cell pellet was resuspended in 1 mL of stain buffer (BD Pharmingen) and incubated with 1 µg of PE-conjugated antimouse CD31 (PECAM-1), CD45, Ter119, Tie2 (CD202b), EpCam (CD326), or FITC-conjugated anti-mouse CD26 antibodies (BD Pharmingen) on ice for 30 min. A small aliquot of cells was incubated with the respective PE-conjugated isotype controls (BD Pharmingen). After washing with 5 mL stain buffer, the cell pellet was resuspended in 1 mL stain buffer containing 1 µL of Nuclear Blue (AAT Bioquest). The cells were sorted on a CytoFLEX SRT-2 cell sorter (Beckman) with a 100-µm nozzle. The viable (Nuclear blue⁻), lineage-negative cells (Lin⁻: CD31⁻, CD45⁻, Ter119⁻, Tie2 EpCam were sorted into ENFs (Lin CD26 and eEPFs $(Lin^-CD26^+).$

Isolation of primary murine dermal fibroblast cell membrane

To isolate cell membrane from primary murine dermal fibroblasts, fibroblasts were washed with PBS, followed by gentle scraping and centrifugation at 300 \times g for 3 min at 25°C. The pellet was suspended in 4 mL of ice-cold isolation buffer (75 mM sucrose, 225 mM mannitol, 30 mM tris-HCl [pH 7.4], 0.5% [w/v] bovine serum albumin, 0.5 mM EGTA, and phosphatase and protease inhibitor cocktail). The suspension was dispersed by ultrasonication (30 W, 1 Hz) in an ice water bath for 3 min to disrupt the cells. After that, the sample was centrifuged at $700 \times g$ for 10 min at 4°C to remove the nuclei and intact cells, followed by supernatant collection. To remove the mitochondria, the supernatant was centrifuged at $10,000 \times g$ for 10 min at 4°C. The precipitate was discarded, and the resulting supernatant was further ultracentrifuged at $100,000 \times g$ for 2 h at 4°C. Last, the fibroblast cell membrane-containing pellet was collected and resuspended in PBS, and the protein in the plasma membrane was assessed using a bicinchoninic acid (BCA) protein assay kit. The obtained fibroblast plasma membrane was stored at -80° C ready for use.

Preparation of FibroMC

FibroMC and FibroMC/siRNA nanocarriers were fabricated by infusing FCM with MC-3 or MC-3/siRNA nanocarrier through microfluidic and extrusion approaches.²¹ The INano L microfluidic mixing instrument (Micro&Nano Biologics) was used to mix the organic and aqueous solution and make the MC-3 or MC-3/ siRNA. The organic solution consisted of MC-3 formulation, which is same as the FDA-approved siRNA drug, patisiran (Onpattro), with DLin-MC3-DMA, cholesterol, DSPC, and DMG-PEG₂₀₀₀ in a mole ratio of 50:38.5:10:1.5.49 The aqueous solution consisted of siRNA and 10 mM citrate buffer (pH 4.0). Next, MC-3 or MC-3/siRNA were fabricated in a microfluidic mixing chip at a flow rate of 12 mL/min, with a 1:3 ratio of organic phase to aqueous phase. The resulting nanocarriers were then dialyzed in 3,500-Da MWCO dialysis tubing (Sigma-Aldrich) against PBS buffer (pH 7.4, 10 mM). Then MC-3 or MC-3/siRNA was mixed with FCM, followed by sequential extrusion through the polycarbonate membrane with a pore size of 400 nm and 200 nm to get FibroMC or FibroMC/ siRNA nanocarrier. To determine the optimal fusion ratio between MC-3 and FCM in FibroMC, MC-3 and FCM were separately labeled with DiO and DiI. The preparation of DiO-labeled MC-3 was similar to that of unlabeled MC-3, with the incorporation of DiO (1% w/w of total lipids) into the lipid phase. FCM was labeled with DiI via incubation at 37°C for 30 min. Then, FibroMC containing a series of different weight ratios of MC-3 to primary mouse dermal fibroblast membrane protein was fabricated, followed by the Förster resonance energy transfer (FRET) analysis.⁵⁰ The emission spectrum of dual fluorescence-labeled FibroMC was recorded from 470 to 650 nm using a microplate reader (Thermo Fisher); the excitation wavelength was 440 nm.

Characterization of FibroMC

To confirm the successful fusion of MC-3 and FCM, they were labeled by DiO (MC-3) and DiI (FCM), respectively. The produced FibroMC nanocarrier was imaged using an Ultra-high Resolution Confocal Microscope (Leica Stellaris 8). The morphology of siEn1loaded MC-3 and FibroMC nanocarriers was observed by a cryotransmission electron microscope (TEM) (200 kV, FEI Tecnai G2 F20, USA). The hydrodynamic size and zeta potential of MC-3 and FibroMC nanocarriers were measured by dynamic light scattering (DLS) using a Zetasizer Nano ZS (Malvern Instruments). The siRNA binding ratio was confirmed by a gel retardation assay. MC-3/siCtrl-FAM and FibroMC/siCtrl-FAM at different N/P ratios were loaded in 1% agarose gel, followed by electrophoresis at 140 V for 30 min. To further evaluate the protection of FibroMC on siEn1, the stability of FibroMC/siEn1 against serum enzyme degradation was evaluated by gel electrophoresis. Free siEn1, MC-3/siEn1, and FibroMC/siEn1 nanocarriers were incubated with 50% FBS at 37°C, and aliquots were collected at different time points. Triton X-100 was then added to release the siEn1, and the mixture was loaded on a 1% agarose gel. RNA fractions were visualized by staining with GelRed. To investigate the stability of FibroMC/siCtrl-FAM, the nanoparticles were maintained in PBS (pH 7.4) at 4°C and analyzed by DLS over 7 days.

Cell viability

Cells were inoculated into 96-well plates at 5 \times 10³ cells/well, cultured under 5% CO $_2$ at 37°C for 12 h, and then treated with MC-3/siCtrl-FAM or FibroMC/siCtrl-FAM. After 24 h, the medium was discarded, and the cells were treated with 10 μL of cell counting kit-8 reagent (Beyotime) per well. Then, the absorbance was determined with a microplate reader at a wavelength of 450 nm.

Proteomics analysis of FibroMC

TMT mass spectrometry was used to analyze the proteins in the FibroMC nanocarrier. Briefly, FibroMC nanocarrier, containing 0.1 mg of membrane protein, were lysed with 300 µL of RIPA supplemented with 1 mM phenylmethanesulfonyl fluoride (Beyotime), followed by ultrasonic treatment on ice (30 W, 1 Hz) for 3 min. Then the samples were centrifuged at $10,000 \times g$ for 10 min, which was repeated twice prior to supernatant collection. The protein concentration was determined by the BCA method (Beyotime). Then 10 µg of protein in each sample was separated by 12% SDS-PAGE, and Coomassie brilliant blue staining was performed using the L00760C eStain LG instrument (Genscript Biotech Corp., Nanjing, Jiangsu, China), and imaged with a Tanon-1600 analysis system (Shanghai Tanon Technology Co., Ltd., Shanghai, China). Next, 50 μg of protein per sample was diluted with a lysis buffer, incubated with 5 mM dithiothreitol at 55°C for 30 min, and cooled on ice to 25°C. The obtained sample was further incubated with 10 mM iodacetamide for 15 min in the dark, followed by acetone supplement $(6\times)$ and storage at -20° C. After 12 h, the precipitate was collected by centrifugation at 8,000 \times g at 4°C for 10 min and reconstituted in triethylammonium bicarbonate (100 μL, 200 mM). Then the sample was mixed with 1 mg/mL trypsin-TPCK (1:50, w/w), followed by incubation at 37°C for 12 h, lyophilization, and then mixing with triethylammonium bicarbonate (50 µL, 100 mM) before treatment with 10 μL of TMTpro label reagent. The reaction was terminated with 5 µL of 5% hydroxylamine for 15 min, followed by sample lyophilization and storage at -80° C. The protein was separated by Agilent 1100 HPLC with an Agilent Zorbax Extend-C18 column. Then, the samples were loaded into Evotip, separated by a 15-cm analytical column, and analyzed using an Orbitrap LC-MS/MS system (Thermo Scientific) with 30 spd.⁵

Bioinformatics analysis

The identified proteins were annotated using the UniProt knowledge base (Swissprot/TrEMBL, http://www.uniprot.org/). The multiomics data analysis tool (OmicsBean) was used to analyze the obtained proteomics data, in which distribution in biological process (BP), cellular components (CCs), and molecular functions (MFs) were assigned to each protein based on GO categories. Kyoto Encyclopedia of Genes and Genomes (KEGG) pathway analysis was performed to enrich high-level functions in the defined biological system.

Cell uptake and affinity

To evaluate the cellular uptake of FibroMC nanocarriers, fibroblasts were seeded on a confocal dish and incubated with FibroMC/siCtrl-

FAM (0.5 µg/mL) for 1 h. The cells were then fixed with 4% paraformaldehyde and stained with DAPI, followed by imaging using a laser scanning confocal microscope (LSM 980, Zeiss). For flow cytometry analysis, fibroblasts were seeded in six-well plates and incubated with FibroMC/siCtrl-FAM (0.5 µg/mL) for 1 h or 3 h. Next, the cells were washed, detached, and analyzed using a flow cytometer (CytoFLEX, Beckman). To explore the cell selectivity of FibroMC nanocarriers, keratinocytes and macrophages (Raw 264.7) were seeded in sixwell plates and incubated with siCtrl-FAM loaded FibroMC (0.5 µg/mL) for 1 h. Next, the cells were washed detached, and analyzed using the same flow cytometer.

Cell uptake mechanism

To explore the mechanism of cell affinity of FibroMC to fibroblasts, western blot analysis was conducted to determine the presence of specific proteins from FibroMC. Proteins resolved by SDS-PAGE were transferred from the gel to polyvinylidene difluoride (PVDF) membranes (Millipore), which were then blocked with 5% BSA for 1 h and incubated overnight with primary antibodies at 4°C. After being rinsed three times for 5 min in Tris-buffered saline containing 0.02% (w/v) Tween 20, PVDF membranes were incubated with goat anti-rabbit IgG-horseradish peroxidase (HRP) secondary antibodies for 1 h. The blots were finally visualized using a Bio-Rad ChemiDoc Touch Imaging System (Bio-Rad). Next, excess (1:100) anti-integrin α2, anti-integrin β1, anti-integrin β3, anti-N-cadherin, anti-Cadherin-11, anti-Catenin β1, anti-Catenin delta1, anti-Caveolin-1, or anti-Talin-1 antibodies were applied to block the corresponding receptors on the surface of FibroMC/siCtrl-FAM nanocarrier. Trypsin was applied to non-specifically digest membrane proteins. 52 After incubation at 37°C for 1 h, FibroMC/siCtrl-FAM suspensions were washed three times with PBS buffer (10 mM, pH 7.4, 4,500 \times g, 10 min per wash) in a centrifugal filter (Pall, 300-kDa molecular weight cutoff) at 4°C, followed by incubation with fibroblasts and analysis by flow cytometry. Regarding chemical inhibition of endocytosis pathways, primary murine fibroblasts were seeded into sixwell culture plates at a density of 1×10^5 cells/well and incubated overnight. Pharmacological inhibitors (1 mM amiloride, 50 μg/mL cytochalasin D, 10 μM colchicine, 10 mM MβCD, 200 nM monensin, or 10 μg/mL chlorpromazine) were added to the cells at 37°C. After 0.5 h, MC-3/siCtrl-FAM or FibroMC/siCtrl-FAM nanocarriers at a concentration of $0.5 \mu g/mL$ were separately added to the wells, which were incubated for another 1 h.53 The cells treated with MC-3/siCtrl-FAM or FibroMC/siCtrl-FAM at 4°C were used to evaluate the effect of temperature on nanocarrier uptake; samples cultured at 37°C without inhibitors were employed as positive controls. The treated fibroblasts were then washed thoroughly with PBS, and FAM-positive cells (1 \times 10⁴ cells) were evaluated by flow cytometry. The data were analyzed using FlowJo (v.10.5).

Lysosomal escape

For investigation of the lysosomal escape of FibroMC, MC-3/siCtrl-FAM or FibroMC/siCtrl-FAM nanocarriers (0.5 μ g/mL) were incubated with fibroblasts seeded on confocal dish for 1, 3, 6, and 9 h. Next, lysosomes were labeled with LysoTracker red DND-99

(Thermo Fisher) and the nuclei were stained with Hoechst (Thermo Fisher), followed by CLSM imaging. Pearson's correlation coefficient was calculated using ZEN 3.6.

En1 silencing and profibrotic effect inhibition

To investigate gene silencing efficiency in all EPF populations, pEPFs were generated by the stimulation of ENFs with PY-60 (10 μM, MCE) for 24 h. Next, eEPFs and pEPFs cells were seeded in sixwell plates for 24 h. MC-3/siEn1 or FibroMC/siEn1 nanocarriers with an siRNA concentration of 1 µg/mL were added to each well. Verteporfin (2 μ g/mL) was set as a positive control. ¹⁵ After incubation for 12 h and 48 h, total RNA was extracted from cell pellets using TRIzol reagent (Invitrogen, USA) according to the manufacturer's instruction. Reverse transcription was performed using the PrimeScript RT Reagent Kit (Takara, Japan). RT-qPCR was performed using the TB Green Fast qPCR Mix Kit (Takara Biomedical Technology Co., Ltd) and the samples were processed through 40 cycles of 95°C for 5 s and 60°C for 30 s after a preheating step of 95°C for 30 s. The relative mRNA expression ($\Delta\Delta$ Ct) of targeted genes was normalized by the expression of β -actin. The primer sequences used for real-time PCR analysis in this study are provided in Table S1.⁵⁴ To investigate the downstream mechanisms following En1 silencing, eEPF and pEPF cells were cultured as described above. MC-3/siEn1 or FibroMC/siEn1 nanocarrier with an siRNA concentration of 1 μg/mL were added to each well. Verteporfin (2 μg/mL) was set as a positive control. After incubating for 48 h, the total RNA was extracted and the relative mRNA expression was quantified by RT-qPCR as detailed above. For protein analysis, cell lysates were collected, and the expression of α-SMA was measured by western blot. Secreted Collagen I and VEGF in the culture supernatant were quantified using ELISA kits (Jiangsu Meimian Industrial Co., Ltd).

Scar prevention evaluation

All animal experiments were conducted following the guidelines for the care and use of laboratory animals. The experimental protocols were reviewed and approved by the Institutional Animal Care and Use Committee (IACUC) at the School of Engineering, Westlake University (AP#21–051).

Twenty male C57Bl6/J (6–8 weeks) mice were purchased from Jiangsu GemPharmatech. All animals were maintained under constant conditions (25 \pm 1°C) with free access to standard diet and drinking water. The animal study referred to the method of a previous study with minor modification. The animals were anesthetized with an intraperitoneal injection of 5% sodium pentobarbital (200 μ L). A full-thickness excision wound was made symmetrically by biopsy (6 mm) and splinted with silicone rings to prevent contraction. Mice with skin wounds were randomly divided into four experimental groups (n = 5 mice per group). The wounds were treated with 10 μ L of PBS (Control group), 10 μ L of 3 mg/mL Verteporfin, MC-3/siEn1, or FibroMC/siEn1, respectively (siEn1: 20 μ g). After treatments, all groups were dressed with transparent Tegaderm (3M) to prevent infection and rehydrate the wounds.

The mice were individually housed in cages to prevent interference among mice. The development of wound healing was recorded by taking a picture on days 3, 7, 10, and14 and measuring the wound area. The weight of the rat was also recorded. The wound healing rate was calculated by dividing the area on day 0 minus area on day n by the area on day 0.

Histological analysis

Histological analysis was performed for the healed skin tissues and organs. Collected samples were fixed in 4% buffered paraformaldehyde, dehydrated, and then embedded in paraffin or OCT compound for slice preparation. The slice sections (5-µm thick) were stained with Masson's trichrome staining (Keygen Biotech), hematoxylin and eosin (H&E, Keygen Biotech), and Sirus red staining according to the manufactures' protocol. The stained skin sections were observed and photographed under an inverted microscope. For Sirius red, polarized light microscopy (Zeiss Axio Scan7) was used to obtain 40× magnification images and analysis of fiber alignment was performed using CurveAlign. 55,56 The strength of alignment ranges from a value of 0 (completely random fiber alignment) to 1 (completely aligned fibers). Additionally, the organs were extracted. The heart, liver, spleen, lung, and kidney were cut into smaller sections, fixed in 4% paraformaldehyde, embedded in paraffin, and sectioned into 5-µm slices. The organ sections were stained with H&E and were visualized by light microscopy for the histological study of toxicity.⁵⁷

Tissue immunofluorescence staining

Healed skin tissues were collected and in 4% buffered paraformaldehyde, dehydrated, and then embedded in paraffin or OCT compound for slice preparation. The embedded skins were sectioned to 4 μ m thick and stained with primary antibodies against En1 (1:1,000, Santa Cruz), α -SMA (1:1,000, Abcam), CD31 (1:1,000, Abcam), and vimentin (1:10,00, Abcam), respectively. En1, α -SMA, CD31, and vimentin signals were visualized using the FITC and Cy3-conjugated secondary antibodies, respectively. Next, the slides were stained with DAPI to visualize the nuclei. All images were acquired on Zeiss Axio Scan7.

Tensile strength testing

Tensile strength tests for unwounded skin and healed skin in different groups were conducted at day 14 and day 28 using a universal testing machine (Cell Scale, UniVert, Canada) equipped with a 20 N load cell. Dorsal skin was harvested and cut into 4-mm by 15-mm strips. Tissue strips were then secured and preloaded to a force of 0.02 N and measured using digital calipers. Finally, the skin was subjected to an extension test to failure, defined by a sharp decrease in stress with increasing strain, at a rate of 18 mm/min. True strain was calculated as the change in length divided by the original gauge length, and true stress was calculated as the force divided by the original cross-sectional area.

Statistical analysis

Unless otherwise stated, data are expressed as mean ± standard deviation. Statistical analyses were performed using GraphPad Prism

version 8 (GraphPad Software Inc.) or ImageJ software. For comparisons between two groups, means were compared using Student's t test (unpaired and two-tailed).

DATA AVAILABILITY

All data supporting the findings of this study are available within the paper and its supplemental information.

ACKNOWLEDGMENTS

This work was supported by the Pioneer and "Leading Goos" R&D Program of Zhejiang (2024SDXHDX0004), National Natural Science Foundation of China (82302379, Q.Z.) and (52233015, J.C.). We acknowledge the support of the New Cornerstone Investigator Program, New Cornerstone Science Foundation. We acknowledge the graphic design from Xinyan Qian and the help from Qinheng Pu.

AUTHOR CONTRIBUTIONS

X.X., Q.Z., and J.C. conceived ideas and designed experiments. X.X. performed experiments, analyzed data, and wrote the manuscript. L.W., X.B., T.C., B.H., and C.J. performed experiments. M.G. and J.Z. contributed reagents, materials, and analysis tools. R.S. and C.S. provided suggestions for methodology. Y.Z., Q.Z., and J.C. provided suggestions for manuscript improvement. Q.Z. and J.C. were responsible for funding acquisition, supervision, and project administration.

DECLARATION OF INTERESTS

The authors declare no competing interests.

SUPPLEMENTAL INFORMATION

Supplemental information can be found online at https://doi.org/10.1016/j.ymthe.2025.07.031.

REFERENCES

- Gurtner, G.C., Werner, S., Barrandon, Y., and Longaker, M.T. (2008). Wound repair and regeneration. Nature 453, 314–321.
- Bayat, A., McGrouther, D.A., and Ferguson, M.W.J. (2003). Skin scarring. Bmj 326, 88–92.
- Sen, C.K. (2021). Human Wound and Its Burden: Updated 2020 Compendium of Estimates. Adv. Wound Care 10, 281–292.
- 4. Jeschke, M.G., Wood, F.M., Middelkoop, E., Bayat, A., Teot, L., Ogawa, R., and Gauglitz, G.G. (2023). Scars. Nat. Rev. Dis. Primers 9, 64.
- Li, D.J., Berry, C.E., Wan, D.C., and Longaker, M.T. (2024). Clinical, mechanistic, and therapeutic landscape of cutaneous fibrosis. Sci. Transl. Med. 16, eadn7871.
- Plikus, M.V., Wang, X., Sinha, S., Forte, E., Thompson, S.M., Herzog, E.L., Driskell, R.R., Rosenthal, N., Biernaskie, J., and Horsley, V. (2021). Fibroblasts: Origins, definitions, and functions in health and disease. Cell 184, 3852–3872.
- Jiang, D., Correa-Gallegos, D., Christ, S., Stefanska, A., Liu, J., Ramesh, P., Rajendran, V., De Santis, M.M., Wagner, D.E., and Rinkevich, Y. (2018). Two succeeding fibroblastic lineages drive dermal development and the transition from regeneration to scarring. Nat. Cell Biol. 20, 422–431.
- Mascharak, S., desJardins-Park, H.E., Januszyk, M., Chen, K., Davitt, M.F., Demeter, J., Henn, D., Griffin, M., Bonham, C.A., Foster, D.S., et al. (2020). Divergent molecular signatures of regeneration and fibrosis during wound repair. Preprint at: bioRxiv. https://doi.org/10.1101/2020.12.17.423181
- Rinkevich, Y., Walmsley, G.G., Hu, M.S., Maan, Z.N., Newman, A.M., Drukker, M., Januszyk, M., Krampitz, G.W., Gurtner, G.C., Lorenz, H.P., et al. (2015). Identification and isolation of a dermal lineage with intrinsic fibrogenic potential. Science 348, aaa2151.
- 10. Mascharak, S., des Jardins-Park, H.E., Davitt, M.F., Griffin, M., Borrelli, M.R., Moore, A.L., Chen, K., Duoto, B., Chinta, M., Foster, D.S., et al. (2021). Preventing Engrailed-1 activation in fibroblasts yields wound regeneration without scarring. Science 372, eaba2374.

- Jiang, D., Christ, S., Correa-Gallegos, D., Ramesh, P., Kalgudde Gopal, S., Wannemacher, J., Mayr, C.H., Lupperger, V., Yu, Q., Ye, H., et al. (2020). Injury triggers fascia fibroblast collective cell migration to drive scar formation through N-cadherin. Nat. Commun. 11, 5653.
- 12. Konieczny, P., and Naik, S. (2021). Healing without scarring. Science 372, 346-347.
- Cao, X., Lu, M., Wang, J., Wang, Y., and Zhao, Y. (2025). Verteporfin-integrated conductive zwitterionic hydrogels for scarless wound management. Nano Today 61, 102659.
- Wei, C., You, C., Zhou, L., Liu, H., Zhou, S., Wang, X., and Guo, R. (2023).
 Antimicrobial hydrogel microneedle loading verteporfin promotes skin regeneration by blocking mechanotransduction signaling. Chem. Eng. J. 472, 144866.
- Wang, P., Peng, Z., Yu, L., Liu, Y., Wang, H., Zhou, Z., Liu, H., Hong, S., Nie, Y., Deng, Y., et al. (2024). Verteporfin-Loaded Bioadhesive Nanoparticles for the Prevention of Hypertrophic Scar. Small Methods 8, 2301295.
- Jiang, D., and Rinkevich, Y. (2021). Converting fibroblastic fates leads to wound healing without scar. Signal Transduct. Target. Ther. 6, 332.
- Setten, R.L., Rossi, J.J., and Han, S.P. (2019). The current state and future directions of RNAi-based therapeutics. Nat. Rev. Drug Discov. 18, 421–446.
- Ren, R., Guo, J., Liu, G., Kang, H., Machens, H.G., Schilling, A.F., Slobodianski, A., and Zhang, Z. (2022). Nucleic acid direct delivery to fibroblasts: a review of nucleofection and applications. J. Biol. Eng. 16, 30.
- Driskell, R.R., and Watt, F.M. (2015). Understanding fibroblast heterogeneity in the skin. Trends Cell Biol. 25, 92–99.
- Chugh, V., Vijaya Krishna, K., and Pandit, A. (2021). Cell membrane-coated mimics: a methodological approach for fabrication, characterization for therapeutic applications, and challenges for clinical translation. ACS Nano 15, 17080–17123.
- Zhou, X., Miao, Y., Wang, Y., He, S., Guo, L., Mao, J., Chen, M., Yang, Y., Zhang, X., and Gan, Y. (2022). Tumour-derived extracellular vesicle membrane hybrid lipid nanovesicles enhance siRNA delivery by tumour-homing and intracellular freeway transportation. J. Extracell. Vesicles 11, e12198.
- Guo, L., Miao, Y., Wang, Y., Zhang, Y., Zhou, E., Wang, J., Zhao, Y., Li, L., Wang, A., Gan, Y., and Zhang, X. (2022). Biomimetic Macrophage Membrane and Lipidated Peptide Hybrid Nanovesicles for Atherosclerosis Therapy. Adv. Funct. Mater. 32, 2204822.
- Li, J., Wu, H., Yu, Z., Wang, Q., Zeng, X., Qian, W., Lu, S., Jiang, L., Li, J., Zhu, M., et al. (2024). Hematopoietic stem and progenitor cell membrane-coated vesicles for bone marrow-targeted leukaemia drug delivery. Nat. Commun. 15, 5689.
- Molinaro, R., Corbo, C., Martinez, J.O., Taraballi, F., Evangelopoulos, M., Minardi, S., Yazdi, I.K., Zhao, P., De Rosa, E., Sherman, M.B., et al. (2016). Biomimetic proteolipid vesicles for targeting inflamed tissues. Nat. Mater. 15, 1037–1046.
- Deng, R., Zhao, R., Zhang, Z., Chen, Y., Yang, M., Lin, Y., Ye, J., Li, N., Qin, H., Yan, X., et al. (2024). Chondrocyte membrane–coated nanoparticles promote drug retention and halt cartilage damage in rat and canine osteoarthritis. Sci. Transl. Med. 16, eadh9751.
- Tang, Q., and Khvorova, A. (2024). RNAi-based drug design: considerations and future directions. Nat. Rev. Drug Discov. 23, 341–364.
- Shalhout, S.Z., Yang, P.-Y., Grzelak, E.M., Nutsch, K., Shao, S., Zambaldo, C., Iaconelli, J., Ibrahim, L., Stanton, C., Chadwick, S.R., et al. (2021). YAP-dependent proliferation by a small molecule targeting annexin A2. Nat. Chem. Biol. 17, 767–775.
- Younesi, F.S., Miller, A.E., Barker, T.H., Rossi, F.M.V., and Hinz, B. (2024).
 Fibroblast and myofibroblast activation in normal tissue repair and fibrosis. Nat. Rev. Mol. Cell Biol. 25, 617–638.
- 29. Gibault, F., Bailly, F., Corvaisier, M., Coevoet, M., Huet, G., Melnyk, P., and Cotelle, P. (2017). Molecular Features of the YAP Inhibitor Verteporfin: Synthesis of Hexasubstituted Dipyrrins as Potential Inhibitors of YAP/TAZ, the Downstream Effectors of the Hippo Pathway. ChemMedChem 12, 954–961.
- **30.** Yampolsky, M., Bachelet, I., and Fuchs, Y. (2024). Reproducible strategy for excisional skin-wound-healing studies in mice. Nat. Protoc. *19*, 184–206.
- 31. Chen, G., Wang, F., Zhang, X., Shang, Y., and Zhao, Y. (2023). Living microecological hydrogels for wound healing. Sci. Adv. 9, eadg3478.

- Limandjaja, G.C., van den Broek, L.J., Waaijman, T., van Veen, H.A., Everts, V., Monstrey, S., Scheper, R.J., Niessen, F.B., and Gibbs, S. (2017). Increased epidermal thickness and abnormal epidermal differentiation in keloid scars. Br. J. Dermatol. 176, 116–126.
- 33. Walmsley, G.G., Maan, Z.N., Wong, V.W., Duscher, D., Hu, M.S., Zielins, E.R., Wearda, T., Muhonen, E., McArdle, A., Tevlin, R., et al. (2015). Scarless Wound Healing: Chasing the Holy Grail. Plast. Reconstr. Surg. 135, 907–917.
- Johnson, K.E., and Wilgus, T.A. (2014). Vascular Endothelial Growth Factor and Angiogenesis in the Regulation of Cutaneous Wound Repair. Adv. Wound Care 3, 647-661
- Veith, A.P., Henderson, K., Spencer, A., Sligar, A.D., and Baker, A.B. (2019).
 Therapeutic strategies for enhancing angiogenesis in wound healing. Adv. Drug Deliv. Rev. 146, 97–125.
- 36. Chen, K., Liu, Y., Liu, X., Guo, Y., Liu, J., Ding, J., Zhang, Z., Ni, X., and Chen, Y. (2023). Hyaluronic acid-modified and verteporfin-loaded polylactic acid nanogels promote scarless wound healing by accelerating wound re-epithelialization and controlling scar formation. J. Nanobiotechnol. 21, 241.
- 37. Xiong, M., Yang, X., Shi, Z., Xiang, J., Gao, H., Ji, S., Li, Y., Pi, W., Chen, H., Zhang, H., et al. (2024). Programmable Artificial Skins Accomplish Antiscar Healing with Multiple Appendage Regeneration. Adv. Mater. 36, 2407322.
- Zhang, Y., Wang, S., Yang, Y., Zhao, S., You, J., Wang, J., Cai, J., Wang, H., Wang, J., Zhang, W., et al. (2023). Scarless wound healing programmed by core-shell microneedles. Nat. Commun. 14, 3431.
- Munisso, M.C., Saito, S., Tsuge, I., and Morimoto, N. (2023). Three-dimensional analysis of load-dependent changes in the orientation of dermal collagen fibers in human skin: A pilot study. J. Mech. Behav. Biomed. Mater. 138, 105585.
- Biggs, L.C., Kim, C.S., Miroshnikova, Y.A., and Wickström, S.A. (2020). Mechanical Forces in the Skin: Roles in Tissue Architecture, Stability, and Function. J. Invest. Dermatol. 140, 284–290.
- 41. Nong, J., Shen, S., Hong, F., Xiao, F., Meng, L., Li, P., Lei, X., and Chen, Y.-G. (2024). Verteporfin inhibits TGF- β signaling by disrupting the Smad2/3–Smad4 interaction. Mol. Biol. Cell 35, ar95.
- Lee, M.-J., Byun, M.R., Furutani-Seiki, M., Hong, J.-H., and Jung, H.-S. (2014). YAP and TAZ Regulate Skin Wound Healing. J. Invest. Dermatol. 134, 518–525.
- Horsley, V. (2022). Cut out that YAPping: Mechanisms to reduce scar formation. Cell Stem Cell 29, 179–181.
- 44. Wei, H., Wang, F., Wang, Y., Li, T., Xiu, P., Zhong, J., Sun, X., and Li, J. (2017). Verteporfin suppresses cell survival, angiogenesis and vasculogenic mimicry of pancreatic ductal adenocarcinoma via disrupting the YAP-TEAD complex. Cancer Sci. 108, 478–487.

- 45. Ji, S., Zhu, Z., Sun, X., and Fu, X. (2021). Functional hair follicle regeneration: an updated review. Signal Transduct. Target. Ther. 6, 66.
- **46.** Yang, X., Xiong, M., Fu, X., and Sun, X. (2024). Bioactive materials for in vivo sweat gland regeneration. Bioact. Mater. *31*, 247–271.
- Talbott, H.E., Mascharak, S., Griffin, M., Wan, D.C., and Longaker, M.T. (2022).
 Wound healing, fibroblast heterogeneity, and fibrosis. Cell Stem Cell 29, 1161–1180.
- 48. Lichti, U., Anders, J., and Yuspa, S.H. (2008). Isolation and short-term culture of primary keratinocytes, hair follicle populations and dermal cells from newborn mice and keratinocytes from adult mice for in vitro analysis and for grafting to immunodeficient mice. Nat. Protoc. 3, 799–810.
- Jayaraman, M., Ansell, S.M., Mui, B.L., Tam, Y.K., Chen, J., Du, X., Butler, D., Eltepu, L., Matsuda, S., Narayanannair, J.K., et al. (2012). Maximizing the potency of siRNA lipid nanoparticles for hepatic gene silencing in vivo. Angew. Chem. Int. Ed. Engl. 51, 8529–8533.
- Piffoux, M., Silva, A.K.A., Wilhelm, C., Gazeau, F., and Tareste, D. (2018).
 Modification of Extracellular Vesicles by Fusion with Liposomes for the Design of Personalized Biogenic Drug Delivery Systems. ACS Nano 12, 6830–6842.
- 51. Wu, T., Hou, X., Li, J., Ruan, H., Pei, L., Guo, T., Wang, Z., Ci, T., Ruan, S., He, Y., et al. (2021). Microneedle-Mediated Biomimetic Cyclodextrin Metal Organic Frameworks for Active Targeting and Treatment of Hypertrophic Scars. ACS Nano 15, 20087–20104.
- 52. Xu, J., Zhang, Y., Xu, J., Liu, G., Di, C., Zhao, X., Li, X., Li, Y., Pang, N., Yang, C., et al. (2020). Engineered Nanoplatelets for Targeted Delivery of Plasminogen Activators to Reverse Thrombus in Multiple Mouse Thrombosis Models. Adv. Mater. 32, 1905145.
- 53. Huang, J.L., Jiang, G., Song, Q.X., Gu, X., Hu, M., Wang, X.L., Song, H.H., Chen, L. P., Lin, Y.Y., Jiang, D., et al. (2017). Lipoprotein-biomimetic nanostructure enables efficient targeting delivery of siRNA to Ras-activated glioblastoma cells via macropinocytosis. Nat. Commun. 8, 15144.
- 54. Györfi, A.H., Matei, A.E., Fuchs, M., Liang, C., Rigau, A.R., Hong, X., Zhu, H., Luber, M., Bergmann, C., Dees, C., et al. (2021). Engrailed 1 coordinates cytoskeletal reorganization to induce myofibroblast differentiation. J. Exp. Med. 218, e20201916.
- Bredfeldt, J.S., Liu, Y., Conklin, M.W., Keely, P.J., Mackie, T.R., and Eliceiri, K.W. (2014). Automated quantification of aligned collagen for human breast carcinoma prognosis. J. Pathol. Inform. 5, 28.
- 56. Liu, Y., Keikhosravi, A., Mehta, G.S., Drifka, C.R., and Eliceiri, K.W. (2017). Methods for Quantifying Fibrillar Collagen Alignment. In Fibrosis: Methods and Protocols, L. Rittié, ed. (Springer), pp. 429–451.
- 57. Xu, X.H., Yuan, T.J., Dad, H.A., Shi, M.Y., Huang, Y.Y., Jiang, Z.H., and Peng, L.H. (2021). Plant Exosomes As Novel Nanoplatforms for MicroRNA Transfer Stimulate Neural Differentiation of Stem Cells in Vitro and in Vivo. Nano Lett. 21, 8151–8159.